



Stellar Wind Contribution to the Origin of Water on the Surface of Oxygen-containing Minerals

Svatopluk Civís¹ , Jiří Kubišta² , Jan Plšek¹ , and Antonín Knížek¹

¹ J. Heyrovský Institute of Physical Chemistry, Czech Academy of Sciences, Dolejškova 2155/3 182 23, Prague, Czech Republic

² Institute of Organic Chemistry and Biochemistry, Czech Academy of Sciences, Flemingovo náměstí 542/2 160 00 Prague 6 Prague, Czech Republic

Received 2024 June 20; revised 2024 September 3; accepted 2024 September 3; published 2024 October 23

Abstract

The origin of water and volatile compounds on planets including Earth is a hotly debated topic in planetary science. For example, many dynamic models suggest that the majority of Earth's water and volatile elements were added from an external source. The stellar wind irradiation of rocky oxygen-containing minerals results in a reaction between H⁺ ions and silicate minerals to produce water and OH, which could explain the presence of water in the regoliths of airless worlds such as the Moon, as well as the water abundances in asteroids. Here, we used the method of high-resolution infrared spectrometry and temperature-programmed desorption (TPD) with mass detection to observe and for the first time quantify water formation on the surfaces of oxygen-bearing minerals. We tested 14 different mineral and natural samples and observed the formation of water on their surfaces upon exposure to H⁺ or D⁺ irradiation. The samples, including two meteorite samples (RAS 445 and SAU 567), were shown to have a water adsorption capacity between 0.09 and 0.7 wt%. The adsorbed water (likely dissociatively adsorbed) remains on the surface at pressures as low as 10⁻⁹ mbar (in the TPD experiment) and temperatures as high as 600 K, which suggests a possible transfer over long distances and timescales. Our article has a general character and demonstrates that any interaction of oxygen-containing minerals with stellar radiation (H⁺ ions) leads to the generation of water adsorbed on the surface of the minerals. The case of the origin of water on Earth is taken as a prime example.

Unified Astronomy Thesaurus concepts: Astrochemistry (75); Solar system (1528); Infrared spectroscopy (2285); Meteorites (1038); Stellar winds (1636); Laboratory astrophysics (2004)

1. Introduction

The origin of water on planets, including Earth, is an open topic in planetary science. Currently, two main views can be distinguished in the literature: water becomes part of the planet during accretion or is later delivered by asteroid and comet impacts (B. Marty 2012). The isotopic composition of hydrogen on Earth is closest to primitive meteorites and at the same time different from the isotopic composition of nebular gas and comets. This suggests that hydrogen and water on Earth "originated from a cosmochemical reservoir that also sourced the parent bodies of primitive meteorites." Moreover, the similar mineral and isotopic composition of the Earth's mantle and the bulk silicate Moon suggests that, whatever its origin, the water on Earth is as old as the Moon formation event (J. J. Barnes et al. 2016). One suggestion is that carbonaceous chondrite (CC) asteroids could have brought water in, as the bulk D/H ratios for most CC types are consistent with those of terrestrial and lunar water (C. M. O. Alexander et al. 2012; L. J. Hallis et al. 2015; J. J. Barnes et al. 2016).

H. Roberts et al. (2004) show that in cold interstellar cores at temperatures less than 50 K, water becomes enriched in deuterium, with D/H ratios reaching as much as 10⁻³–10⁻². Water in the protosolar cloud would therefore have had a high D/H ratio. However, when the water was incorporated into the hotter region of the protosolar disk, isotopic reactions with other hydrogen-bearing species (such as H₂O + HD ⇌ HDO + H₂)

would have lowered the D/H ratio significantly (F. Hersant et al. 2001).

The D/H isotopic ratio is used as the main discriminant in discerning the origin of Earth's water. The ratio is usually expressed as δD in ‰ as D enrichment relative to the D/H ratio in ocean water.

Both the D/H ratios in the Sun's natal disk and Jupiter's are very low at $\approx 21 \times 10^{-6}$ ($\delta\text{D} \approx -800\text{\textperthousand}$). On the contrary, the D/H ratio of Earth's oceans is $\approx 156 \times 10^{-6}$ (standard $\delta\text{D} \approx 0\text{\textperthousand}$). Comets, such as the 67P/Churyumov-Gerasimenko comet, generally show high D/H ratios (up to 530×10^{-6} , $\delta\text{D} \approx 2400\text{\textperthousand}$; K. Altwege et al. 2015). Even though historically considered as possible sources of terrestrial water due to their high water content, considerations of the presence of other ices and their isotopic composition make comets an unlikely source of the majority of Earth's water (J. A. Paquette et al. 2021; A. Izidoro & L. Piani 2022).

Furthermore, volatiles delivered to Earth are presumed to originate from C-type asteroids (S. N. Raymond et al. 2006; K. J. Walsh et al. 2011; D. P. O'Brien et al. 2014; S. N. Raymond & A. Izidoro 2017). Especially, CM chondrites are a particularly close match to Earth in terms of the D/H ratio (B. Marty 2012; F. M. McCubbin & J. J. Barnes 2019). Due to their high water content, they are therefore considered as an important source of volatiles (A. Morbidelli et al. 2000). However, the diversity of CCs in the meteorite record makes CM chondrites as the sole source of water on Earth unlikely (V. Meadows et al. 2020). The D/H ratios of the deep mantle are also lighter than the standard mean water ratios, implying a different source of hydrogen and water on Earth (B. Marty 2012).

Solar wind irradiation of rocky materials enables a reaction between the incident H and silicate minerals, resulting in the



Original content from this work may be used under the terms of the [Creative Commons Attribution 4.0 licence](#). Any further distribution of this work must maintain attribution to the author(s) and the title of the work, journal citation and DOI.

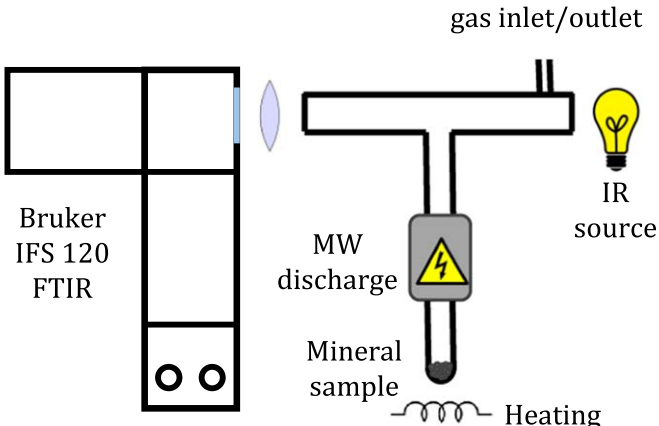


Figure 1. Schematic setup involving a combination of microwave (MW) discharge with absorption Fourier-transform infrared spectroscopy (FTIR) analysis. Gas-phase IR spectra were recorded using a Bruker IFS 120 spectrometer with a resolution of 0.03 cm^{-1} . Deuterium atoms were generated using a MW magnetron discharge.

formation of water (P. Lucey et al. 2006; J. P. Greenwood et al. 2011; A. S. Ichimura et al. 2012; Y. Liu et al. 2012; J. P. Bradley et al. 2014; C. Zhu et al. 2019). The formed water after its formation becomes trapped in the surface damage layer of the mineral (J. P. Bradley et al. 2014). It has been proposed that this phenomenon is the source of water in the lunar regolith (C. M. Pieters et al. 2009; J. M. Sunshine et al. 2009; J. L. Bandfield et al. 2018). Such formation of water has been shown in the laboratory previously (P. Lucey et al. 2006; J. P. Bradley et al. 2014). This mechanism therefore holds potential for the explanation of the origin of some of Earth’s water reservoir. The efficiency of this process has not been established yet. A possible source of such water on Earth could be the regolith of silicate-rich asteroids and interplanetary dust particles (IDPs) (L. Daly et al. 2021). Together with primitive chondrite meteorites, these materials make up to 99% of the present-day extraterrestrial mass flux on Earth, but could also have been abundant in the past (see L. Daly et al. 2021 and references therein).

The process of water formation on mineral surfaces by solar wind could also explain the presence of water on nominally anhydrous minerals on asteroids (J. L. Bandfield 2002).

To investigate the process of water formation on the surface of oxidic materials and water abundances, we used the technique of surface bombardment with hydrogen or deuterium atoms and ions. The technique of discharge irradiation was used as a complement, and the adsorption, desorption, and displacement kinetics of H_2O on the surface of oxygen-containing minerals were investigated using temperature-programmed desorption (TPD) and molecular-beam techniques.

Thus, two different detection techniques, high-resolution Fourier-transform infrared spectrometry (FTIR) and TPD with mass spectrometry, were used to measure the abundance of water and OH radical molecules within minerals.

2. Experiments

This paper discusses the possible formation of water on oxygen-containing minerals by stellar wind and its subsequent transport to planets. First, we performed a microwave (MW) discharge experiment with FTIR analysis and a sputter gun irradiation with TPD analysis, both to show the formation of water on mineral surfaces. Both these experiments include a

mineral sample bombarded by hydrogen/deuterium ions, which, among other possibilities, react with surface oxygens in the mineral lattice and form water molecules.

Next, we experimentally evaluated the adsorption capacity of selected minerals through gas-phase Fourier IR spectrometry. This was to show the ability of minerals to retain some water during transport through interplanetary space and deliver it to planets. Water has been shown to dissociatively adsorb on the surface of olivine and remain bonded as OH at temperatures as high as 900 K, suggesting a possible origin of water on asteroids and comets from the accretion disk (L. Vattuone et al. 2013).

2.1. Formation of Water with MW Discharge Monitored with FTIR

The MW discharge experiment consisted of a closed sample cell filled with molecular hydrogen/deuterium gas and a solid mineral sample. A MW discharge was induced in the cell, which produces hydrogen/deuterium atoms both in their neutral and excited states. These atoms then interact with oxygen in the mineral lattice, forming water. The cell was placed in the optical path of a light source, heated to evaporate the surface water, and high-resolution gas-phase FTIR spectrometry was used to detect H_2O in the gas phase of the sample. A schematic drawing of the experiment is shown in Figure 1 and a photo in Figure 15 in Appendix B. In detail, first, we conducted a MW discharge experiment to generate hydrogen/deuterium atoms/ions from molecular hydrogen/deuterium. To achieve this, we utilized a quartz finger connected to a borosilicate glass absorption cell. The cell was equipped with CaF_2 optical windows and a vacuum valve. Connected to the finger was a MW cavity resonant holder, cooled by water, positioned close to the sample surface. A magnetron MW power source was connected with a coaxial cable. This source can be continuously adjusted, and the maximum power used was 75 W at a frequency of 2.45 GHz. We optimized the frequency circuit of the cavity with regard to both MW power and the optimal spatial distribution of the discharge within the quartz tube.

At the beginning of the experiment, mineral samples in powdered form (100 mg) were introduced into the quartz finger and evacuated at a temperature of 600 K over a period of 12 hr through a vacuum valve at pressures of 10^{-3} mbar. The cell was then filled with 1 mbar of molecular H_2 or D_2 and the discharge was run for 2 hr. Following this, the gas was evacuated to 10^{-3} mbar and the cell was closed. After that, the finger with the sample was heated (inside an oven) to a temperature of 600 K and the released water from the surface was detected in the gas phase using high-resolution FTIR.

In all experiments the absorption beam from an external radiation source was focused through the absorption glass cell (see Figure 1) to the entrance aperture of the interferometer using a CaF_2 lens. The absorption spectra were recorded using a Bruker IFS 120 spectrometer (Bruker, Germany), equipped with a KBr beamsplitter and an InSb detector. For each measurement, a total of 100 scans were coadded at a spectral resolution of 0.03 cm^{-1} in the range $800\text{--}5000 \text{ cm}^{-1}$. To calculate the partial pressures of each detected species, the collected spectra were fit with the `spectr` library (A. N. Heays 2022). The library fits HITRAN molecular line parameters (including temperature and pressure-induced spectral effects) to existing data and calculates column densities

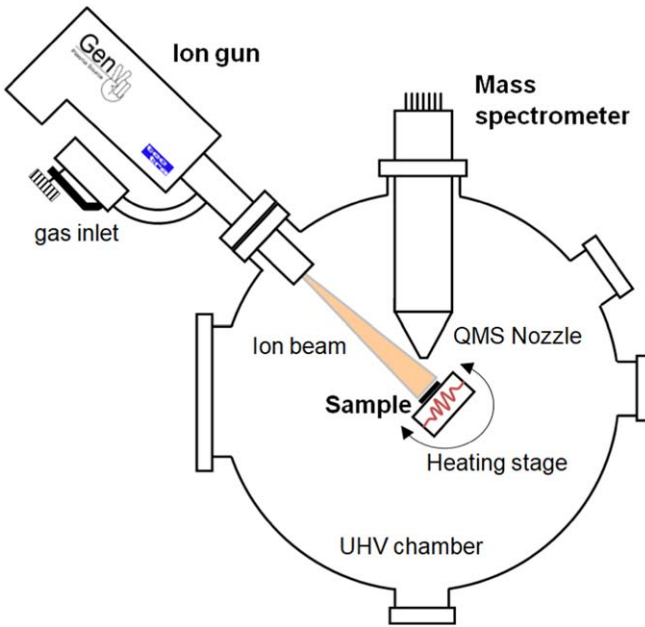


Figure 2. Top view of the ultra-high vacuum chamber used for the TPD experiments. The residual pressure in the chamber during TPD was lower than 5×10^{-10} mbar. An ion gun for sample bombardment and quadrupole mass spectrometer were connected to the chamber.

(I. E. Gordon et al. 2022). Column densities and the optical path of the cell were used to calculate the partial pressure using the ideal gas law. This approach enables rapid data analysis without the need for analytical calibration during the data-evaluation process. Blank measurements (i.e., an empty quartz cell without sample) were performed for all experiments and no formation of water was observed.

2.2. Formation of Water with a Sputter Gun Monitored through TPD

An alternative approach for observing the formation of water is the utilization of a sputter gun and subsequent monitoring with TPD. The desorption experiments were carried out in an ultra-high vacuum chamber made of stainless steel. The chamber is schematically shown in Figure 2. The chamber was permanently pumped using a turbomolecular pump. The whole TPD system consists of an ion gun (IonEtch sputter gun, TecTra GmbH), used for irradiation of the sample with hydrogen or deuterium ions, a quadrupole mass spectrometer (RGA-200, QMS), for ion detection, housed in a differentially pumped tube, which is terminated by a nozzle with an aperture of 3 mm on the front end, viewports, and a sample holder. In total, six experiments were performed with a different composition each time. Details are described along with the resulting plots below. All samples were loaded on a sample holder in the vacuum chamber and dried in vacuum at 600 K and $<5 \times 10^{-10}$ mbar. After drying and cooling, the samples were sputtered with hydrogen/deuterium ions first, which should result in water formation on the surface. Bombardment of samples was done at 8.5×10^{-5} mbar by ions with an energy of 0.5 kV for 20 minutes with a total ion current of $\sim 10 \mu\text{A}$. The samples were then heated by the e-beam method from a tungsten cathode installed 4 mm below the sample holder equipped with a K-type thermocouple. The temperature of the sample was continuously monitored using the K-type thermocouple, which also provided feedback for the TPD computer

control system. TPD spectra were obtained at a constant sample heating rate of 2 K sec^{-1} , and the desorption rate of the selected m/z masses was monitored quantitatively using the quadrupole spectrometer. To increase the sensitivity of the mass spectrometer detector during TPD, a nozzle was used that approached the surface of the sample (at a distance of about 1 mm), which allowed collection of the desorbed products from the sample and improved the signal-to-noise ratio. We use isotopic labeling in order to differentiate between water adsorbed from gas residues and water formed as a consequence of ion bombardment.

2.3. Water Adsorption Capacity with FTIR

The specific adsorption capacity of different minerals used in this study was determined through FTIR measurement. A known mass of a sample (100 mg) was introduced into a sample finger, as shown in Figures 1 and 15 in Appendix B. Then the sample was heated (600 K) under vacuum for 2 hr to remove trace water (attained pressure 0.001 Torr). The dried sample was then cooled to ambient temperature and exposed to a saturated pressure of D_2O (18 Torr) for 1 hr. Subsequently, the sample was evacuated at room temperature until the gas phase contained no detectable D_2O (10^{-3} mbar). Finally, the sample was heated to 600 K to release the adsorbed heavy water. Gas-phase spectra were measured, analyzed, and the adsorption capacity of the mg D_2O /mg sample was calculated. Infrared spectra were collected using a Bruker IFS 120 spectrometer as described above.

3. Results and Discussion

3.1. Formation of Water in MW Discharge

The formation of water was observed by irradiation of the sample surface by hydrogen ions produced in a MW discharge. The formation of excited H atomic species was observed, which implies the presence of H^+ ions as well. An experimental H atomic spectrum is shown in Figure 16 in Appendix C. Fourteen assorted minerals and catalysts were tested for water formation activity. These included synthetic minerals, such as TiO_2 anatase and nanorutile from Aldrich, in-house synthetic TiO_2 P25 anatase, synthetic Fe_2O_3 , montmorillonite, kaolinite, and Al_2O_3 (Sigma Aldrich). Two meteorites were also included: Ramlat as Sahmah 445 (RAS 445) and Sayh al Uhaymir 567 (SAU 567). Tested natural samples included diallage (collected in Dzikowies, Poland), olivine (grains in basalt, collected in Smrčí u Semil, Czechia), oligoclase (collected in Vlastějovice, Czechia) and augite (collected in Bořislav, Czechia).

Figure 3 shows spectra of D_2O formed on the surface of mineral samples listed in Table 1 in a MW discharge. The spectra show the IR absorption bands of D_2O . Its formation was observed in all samples except TiO_2 -P25, as discussed below. All the samples represent oxygen-containing minerals. Figure 3 shows three IR spectra. The top spectrum shows D_2O reference bands. The middle and bottom spectra depict the formation of D_2O on the surfaces of Fe_2O_3 and Al_2O_3 . Other results are shown in Appendix A. Figure 12 shows water formation on the surface of montmorillonite, augite, and kaolinite. Figure 13 shows water formation after irradiation of oligoclase, olivine, and diallage, all of them natural minerals. Finally, Figure 14 shows IR spectra of water formed after

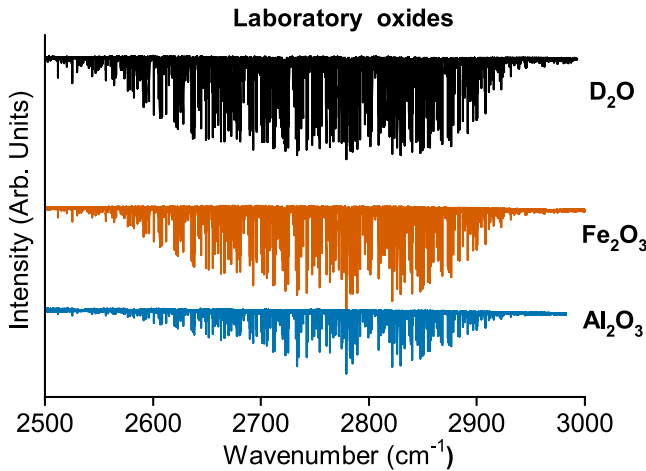


Figure 3. Gas-phase high-resolution D₂O absorption spectra obtained in the spectral range of the OD stretch mode for several oxygen-containing oxides after surface MW bombardment by deuterium atoms. The amount of heavy water yield is strongly affected not only by elemental composition but also by different types of surface activity.

Table 1
List of Tested Minerals for the Production of Water in Our Experiments

No.	Mineral	Forms H ₂ O in MW Discharge
1	Fe ₂ O ₃	✓
2	TiO ₂ P25 anatase	✗
3	Montmorillonite	✓
4	Kaolinite	✓
5	Augite	✓
6	Diallage	✓
7	Oligoclase	✓
8	Al ₂ O ₃	✓
9	Olivine	✓
10	RaS 445 meteorite	✓
11	SaU 567 meteorite	✓
12	TiO ₂ nanorutile	✓
13	TiO ₂ anatase	✓
14	Ti ¹⁸ O ₂	✓

Note. Activity for the formation of H₂O in the MW discharge experiment is indicated.

irradiation of the two meteoritic samples, RAS 445 and SAU 567.

3.2. Special Case: TiO₂

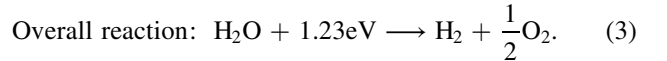
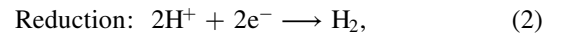
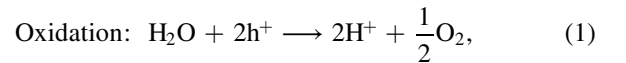
As was shown in Table 1, D₂O molecules were identified in all experiments related to the application of MW discharge, except for TiO₂ P25 {101} anatase. In this case, as shown in Figure 4, even after multiple repetitions of the experiment, we were unable to detect any water formed on the surface of the TiO₂ {101} sample.

During the experiment, the sample of the oxide material is exposed not only to a strong current of H, H⁺, and molecular hydrogen in excited Rydberg states (see Figure 16 in Appendix C), but also to intense visible and UV radiation generated in the hydrogen discharge.

The overall photoelectrochemical water splitting reaction (2H₂O → 2H₂ + O₂) was achieved on a TiO₂ photoanode as early as 1972 (A. Fujishima & K. Honda 1972), with many studies following (R. Li et al. 2015; H. Eidsvag et al. 2021).

Studies on the photoelectric activity of TiO₂ show that, in particular, anatase dominated with {101} facets is highly effective for hydrogen production from water splitting (H. G. Yang et al. 2008; K. M. Macounová et al. 2017).

Generally, photocatalytic water splitting involves the conversion of water (H₂O) into hydrogen (H₂) and oxygen (O₂) through the use of a catalyst and natural light (in our experiment visible and UV light generated in the hydrogen MW discharge). In the initial step, under irradiation, electron–hole pairs are generated in a semiconductor photocatalyst, prompting the excitation of electrons from the valence band (VB) to the conduction band. In the second step, charge separation occurs as the photogenerated electrons migrate toward the surface. Upon reaching the surface, the photogenerated holes react with water to produce oxygen and H⁺, and the electrons present recombine with the H⁺ to produce H₂. The redox and oxidation reactions on the photocatalyst's surface are represented by the following equations:



The process of water splitting is highly endothermic, with a reaction Gibbs free energy of 1.23 eV (corresponding to light with a wavelength 1008 nm). To initiate the reaction, the photocatalyst must have a band gap greater than 1.23 eV, typically between 1.6 eV and 1.8 eV in practice, considering overpotentials. However, the band gap should not be excessively high, as it would diminish the photocatalyst's ability to absorb visible light. In addition to an appropriate band gap, the conductive band minimum must be more negative than the redox potential of H⁺/H₂ (0 V versus normal hydrogen electrode), and the VB maximum must be more positive than the redox potential of O₂/H₂O (1.23 V). Another very important factor for photocatalyst efficiency is the recombination time, i.e., the duration for an electron–hole pair to recombine. If the electron–hole pair recombines before reaching the surface, the reaction is prevented. Other important material properties include crystallinity, dimensionality, pH dependency, and band gap. Besides these properties, TiO₂ is also known to freely exchange oxygen atoms in CO₂ at room temperature (D. C. Sorescu et al. 2014; S. Civiš et al. 2016) and reduce CO₂ through methanogenesis to generate CH₄ or other hydrocarbons on the surface (S. Civiš et al. 2017; S. Civiš 2021). The usage of the isotopically labeled samples in this study was inspired by the referenced papers.

One other aspect of the photocatalytic reduction process concerns the number of required electrons. R. Li et al. (2015) report a lack of O₂ evolution from water splitting on anatase TiO₂ during the initial stage of the reaction. This may be attributed to the existence of trapped states in the bulk and surface regions. The presence of these states reduces the overpotential for water oxidation, making the photogenerated holes more inclined to oxidize the H₂O molecules and produce the OH radical in a two-electron process. This process requires less potential than a four-electron process to directly produce O₂. UV light with high intensity can gradually reduce the deep trapped states near the VB of anatase TiO₂, increasing the overpotential for water oxidation and enabling H₂O oxidation

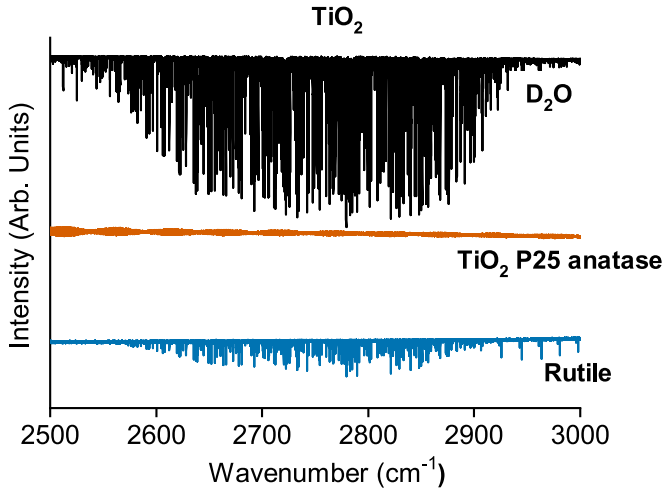


Figure 4. MW-FTIR experiment, in which TiO_2 P25 anatase was bombarded by deuterium atoms generated in a MW plasma. The gas-phase absorption spectrum of D_2O is depicted for comparison (in black).

through the four-electron process to yield O_2 , which appears in the reaction later on.

Therefore, it is safe to assume that water molecules generated on the surface of TiO_2 in the atmosphere of hydrogen during our discharge experiment are simultaneously decomposed by UV radiation generated by the MW discharge, likely through the simplest reduction process resulting in the formation of H_2 molecules. In our MW discharge experiment, it was technically infeasible to separate the sample bombarded by H^+ ions from the relatively strong UV radiation generated within the hydrogen MW discharge.

3.3. TPD Experiment

Another approach to observe the experimental formation of water is the utilization of a sputter gun and irradiation of a mineral sample directly by hydrogen/deuterium ions. Six variants of the experiment were performed, as shown in the Table 2.

3.3.1. Formation of H_2^{18}O with Sputter Gun Monitored with TPD on Ti^{18}O_2

First, a Ti surface was cleaned by bombardment with Ar^+ ions (4 kV, 10 μA , 10 minutes) at 300 K. After purification, TPD spectra were recorded for control. On the cleaned Ti surface TiO_2 oxide was formed by bombardment with $^{18}\text{O}^+$ ions (500 eV, 6 μA , 10 minutes); the layer of the formed oxide with isotopically labeled oxygen was again checked by TPD. In the next step, the surface of the formed oxide was bombarded with H^+ ions (500 eV H_2 , 10⁻⁶ Torr, 6 μA , 10 minutes). The water formed by the reaction of hydrogen ions with titanium dioxide was finally released during the final TPD measurement. The result is shown in Figure 5.

3.3.2. Formation of D_2^{16}O and H_2^{18}O with Sputter Gun Monitored with TPD on $\text{Ti}^{16/18}\text{O}_2/\text{Au}$

Here, 50 mg of $\text{Ti}^{16}\text{O}_2/\text{Ti}^{18}\text{O}_2$ was finely ground in a friction pan. Then a suspension was prepared by adding approximately 1 ml of acetonitrile. The acetonitrile suspension was dripped onto an Au plate mounted on a tantalum sample holder. After evaporation of the solvent, the sample was placed

Table 2
List of Experiments Performed with the TPD Method

No.	Mineral	Ion	Product
1	Ti^{18}O_2	H^+	H_2^{18}O
2	$\text{Ti}^{18}\text{O}_2/\text{Au}$	H^+	H_2^{18}O
3	$\text{Ti}^{16}\text{O}_2/\text{Au}$	D^+	D_2^{16}O
4	Al_2O_3	D^+	D_2^{16}O
5	Fe_2O_3	D^+	D_2^{16}O
6	FeTiO_3	D^+	D_2^{16}O

Note. The table shows the solid mineral, the ion with which the material was irradiated, and the detected product.

in a vacuum chamber and evacuated to 10⁻⁷ mbar. After 24 hr, the sample was transferred from the load lock chamber to the TPD chamber (10⁻⁹ mbar). The sample was initially checked for contamination by TPD ramp. The temperature was measured using a thermocouple attached to the sample holder.

In the next step the surface was bombarded by D^+ or H^+ ions (500 eV D_2 or H_2 10⁻⁶ Torr, 6 μA , 10 minutes) to create water molecules. The exposed sample surface was approximately 7 mm in diameter, and the spot size of the incident ion beams was >5 cm. Finally, TPD spectra of the created heavy water D_2O ions m/z 20 and HDO ions m/z 19 were recorded.

Two experiments were conducted using this setup. First, Ti^{16}O_2 was irradiated with D^+ and the formation of D_2^{16}O was observed. The result is shown in Figure 6, which shows the released D_2^{16}O in millibars.

The second experiment in this setup was the formation of H_2^{18}O . Here, in-house synthesized Ti^{18}O_2 was used and irradiation of H^+ was employed. As expected, the formation of H_2^{18}O was observed. The resulting TPD spectrum is shown in Figure 7.

3.3.3. Formation of D_2^{16}O with Sputter Gun Monitored with TPD on Mineral Oxides

In a manner similar to the experiment described above, acetonitrile solutions of Al_2O_3 , Fe_2O_3 , and ilmenite were dripped onto an Au foil and irradiated with D^+ ions. Again, the formation of D_2O was observed, further confirming the formation of water on the tested minerals. The resulting spectra are shown in Figures 8–10.

4. The Origin of Water on Planets

4.1. Water on Planets

The isotopic composition of water on Earth and other terrestrial planets can provide clues about its origin and persistence. The ratio of deuterium to hydrogen (D/H) can indicate, for example, the degree of water loss or fractionation that occurred during planetary evolution. The D/H ratio of Earth's oceans is about 1.6×10^{-4} , while that of Venus's atmosphere is about 1.9×10^{-2} , suggesting that Venus lost most of its water through atmospheric escape. The D/H ratio of Mars's atmosphere is about 4.5×10^{-4} , indicating that Mars also lost a significant amount of water over time.

The amount of water on each terrestrial planet is also uncertain and may have changed over geological history. Earth has about 2.3×10^{21} kg of water, which is about 0.04% of its mass. Venus may have had at least 0.3% of Earth's hydrosphere in the past, but now has only about 200 mg kg⁻¹

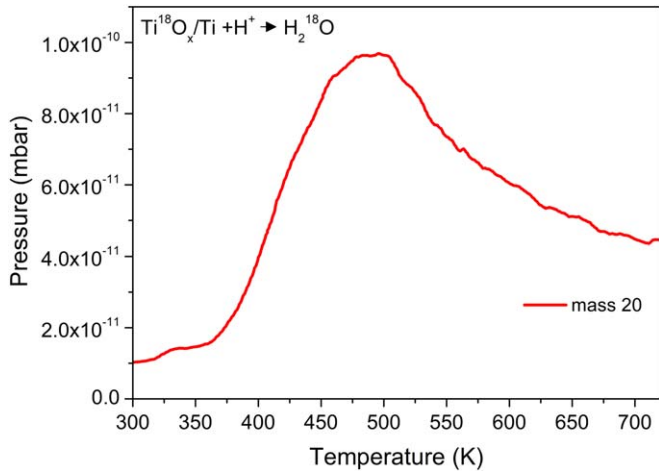


Figure 5. Spectrum from the in situ prepared Ti^{18}O_2 from Ti foil by bombardment with $^{18}\text{O}^+$ ions as described. The prepared titanium oxide was later bombarded with hydrogen ions for 20 minutes. The resulting TPD shows the produced H_2^{18}O (20 m/z) molecules.

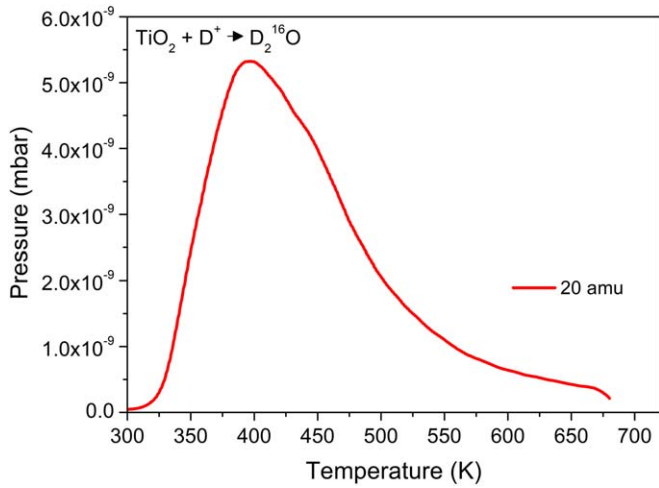


Figure 6. Spectrum of TPD from the Ti^{16}O_2 prepared as a suspension. The suspension on Au foil was bombarded with deuterium ions for 20 minutes. The resulting TPD shows the produced D_2^{16}O (20 m/z) molecules.

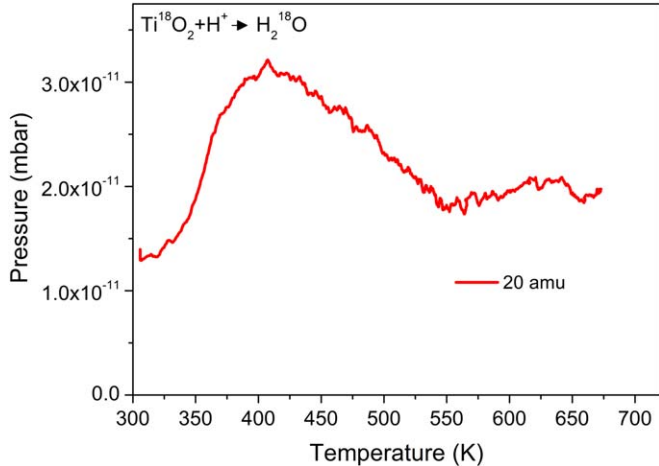


Figure 7. Spectrum of TPD from the Ti^{18}O_2 prepared from a suspension. Ti^{16}O_2 on Au foil was bombarded with hydrogen ions for 20 minutes. The resulting TPD shows the produced H_2^{18}O (20 m/z) molecules. Note that the signal is more noisy as a result of isotope exchange of isotopically marked oxide during storage.

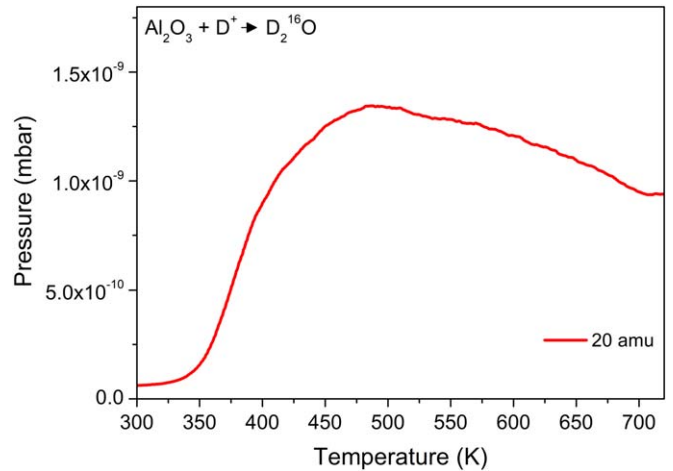


Figure 8. Temperature-programmed desorption spectrum of D_2^{16}O molecules for the Al_2O_3 sample on Au foil, which was bombarded with D^+ ions for 10 minutes.

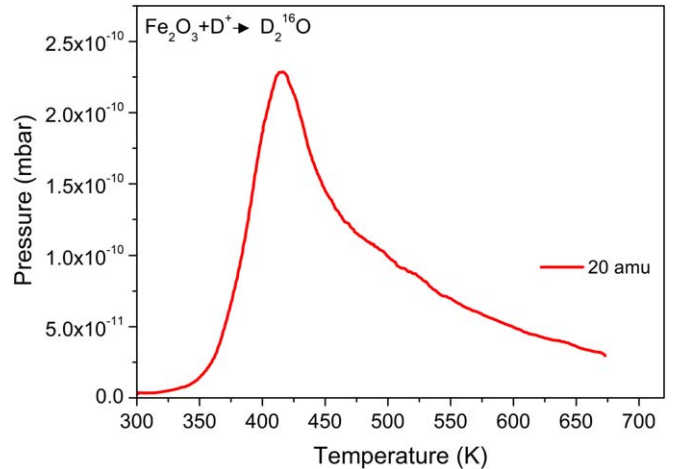


Figure 9. Temperature-programmed desorption spectrum of D_2^{16}O molecules for the Fe_2O_3 sample on Au foil, which was bombarded with D^+ ions for 20 minutes.

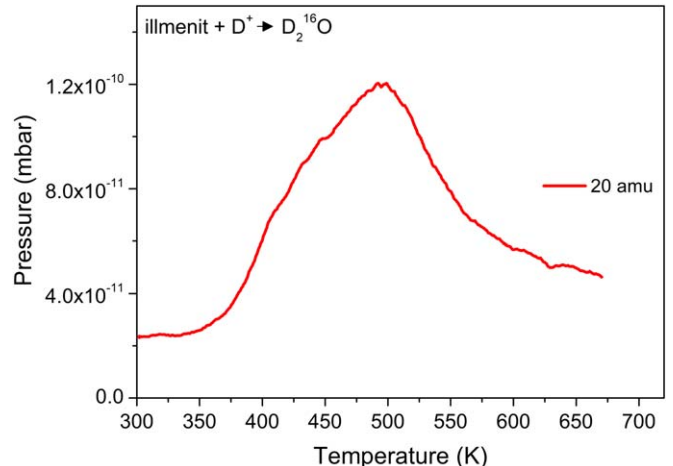


Figure 10. Temperature-programmed desorption spectrum of D_2^{16}O molecules for the FeTiO_3 sample on Au foil, which was bombarded with D^+ ions for 20 minutes.

of water vapor in its atmosphere. Mars may have had a global ocean covering about a third of its surface in the past, but now has only about 3×10^{16} kg of water ice at its poles and subsurface. Mercury and the Moon appear to be very dry, but may have some water ice trapped in permanently shadowed craters near their poles.

4.2. D/H Ratio

There are two end-member possibilities for the presence of water during accretion of planets. One possibility is that temperatures were too high in the inner solar system for hydrous phases to exist in the accretion disk, so the terrestrial planets accreted “dry.” The other possibility is that the terrestrial planets accreted “wet” from hydrous materials that formed or migrated in the inner solar system. Similarly, the possible sources of water can be divided into endogenous and exogenous categories. Endogenous sources include direct adsorption of water from gas onto grains in the accretion disk and accretion of hydrous minerals forming in the inner solar system. Exogenous sources include delivery of water by asteroids, comets, and planetary embryos from beyond the snow line. Explanation of the origin and isotopic composition of Earth’s volatiles based on isotopic ratios of major elements, such as C/H, C/N, C/S, etc., “involves a combination of parent body processing, core formation, catastrophic atmospheric loss, and partial replenishment by late veneer” (M. M. Hirschmann 2016).

4.3. Solar Wind

Through observations and laboratory experiments, it has been established that when rocky materials are exposed to solar wind irradiation, a chemical reaction occurs between hydrogen ions and silicate minerals, resulting in the formation of hydroxyl (OH) and water molecules (K. L. Laferriere et al. 2022; P. G. Lucey et al. 2022). This has been investigated by M. J. Schaible & R. A. Baragiola (2014), who studied hydrogen implantation on amorphous SiO₂ and olivine with a proton beam. Although they observed the formation of OH (in SiOH complexes), they found no evidence of molecular water formation. We used olivine in our experiment, as well, and in principle one could expect to observe the same results from both experiments, even though the proton sources were different. Another striking difference in the experiments, though, is the detection method. M. J. Schaible & R. A. Baragiola (2014) use transmission FTIR on a solid sample and observe Si–OH absorption bands in their sample. Naturally, this detection technique is limited to a lower resolution ($4\text{--}8\text{ cm}^{-1}$). Our analysis is based on evaporating the water that forms on the surface and the subsequent measurement of gas-phase FTIR absorption spectra with a resolution 0.03 cm^{-1} . This gives us a much lower detection limit. On the other hand, we are unable to observe the complexes and adsorbates on the solid sample, giving us no insight into the formation mechanism. A similar experiment was performed by Q. Jiang et al. (2024), who studied hydrogen implantation on the surfaces of olivine, orthopyroxene, and quartz. They found that the hydrogen saturation level by implantation is much higher than the bulk solubility limit and also that the saturation capacity depends on the nature of the mineral, very much in line with our results. The samples were analyzed with the nuclear resonance reaction analysis technique, and the authors

observed hydrogen depth profiles in the samples. Even though the authors did not directly observe any formation of water, they estimate the production of water on Earth through this process upon the assumption that all implanted hydrogen is converted into molecular H₂O, which is between 40 and 400 ocean masses for $0.1\text{--}1\text{ }\mu\text{m}$ dusts in about 100 yr. As the authors discuss, this calculation utilizes multiple simplifications and constraints, but can be regarded as an upper limit. In contrast, we observe directly the water formation and can relate the observed value to the sample loading. On the other hand, we have no direct insight into the surface formation mechanism and, even though we do not need as many parameters for the calculation, our values are rather more empirical.

The water observed in our experiment and formed by solar wind can become entrapped within an upper layer, typically 20–200 nm in thickness (J. P. Bradley et al. 2014). This offers a plausible explanation for the presence of water in regoliths on airless celestial bodies like the Moon. Additionally, the implantation of solar hydrogen could elucidate why nominally anhydrous minerals in asteroids exhibit water abundances of several hundred parts per million by weight (J. L. Bandfield et al. 2018; L. Piani et al. 2021).

Compelling evidence for these reactions is further corroborated by the detection of OH bonds and the inferred water contents, which can reach up to 1 mol% on the surfaces of IDPs that have been exposed to solar wind irradiation. These findings are also substantiated by the production of water in minerals during laboratory experiments simulating space weathering (J. P. Bradley et al. 2014). This body of evidence suggests that a volatile reservoir, characterized by isotopic similarity to the solar wind, might have existed within the solar system and potentially contributed to the formation of Earth’s oceans.

5. Adsorption Capacity of Minerals and the Origin of Water on Planets

The experiments above confirmed that water can be formed on the surfaces of minerals as they travel through space and interact with the stellar wind. A visualization of this process is provided in Figure 11. This section contains a very simplified extrapolation of the experimental results to the magnitude of water delivery to planets.

Using the FTIR-determined water adsorption capacities, a ballpark estimation of the required mass delivery to explain the Earth’s water budget can be obtained. Earth’s hydrosphere contains $\sim 1.46 \times 10^{21}$ kg of H₂O, the vast majority of which resides in oceans. Water contained in the mantle is poorly constrained, and can contain up to 4×10^{21} kg of water (C. Thomas 1994).

Using values for the adsorption capacity of minerals from Table 3 and the amount of water on the contemporary Earth, the amount of material required to deliver that amount of water can be calculated as

$$m_{\text{tot}} = m_{\text{H}_2\text{O}} w_{\text{H}_2\text{O}}, \quad (4)$$

where m_{tot} (in kilograms) is the total delivered mass, $m_{\text{H}_2\text{O}}$ is 1.46×10^{21} kg, and $w_{\text{H}_2\text{O}}$ is the maximum amount of water adsorbed on a gram of mineral determined from our experiment from Table 3 above. The hypothetical amount of material required to bring in one equivalent of Earth’s ocean water is then also shown in Table 3. It is clear that more water exists on Earth and that the impacting material has a different

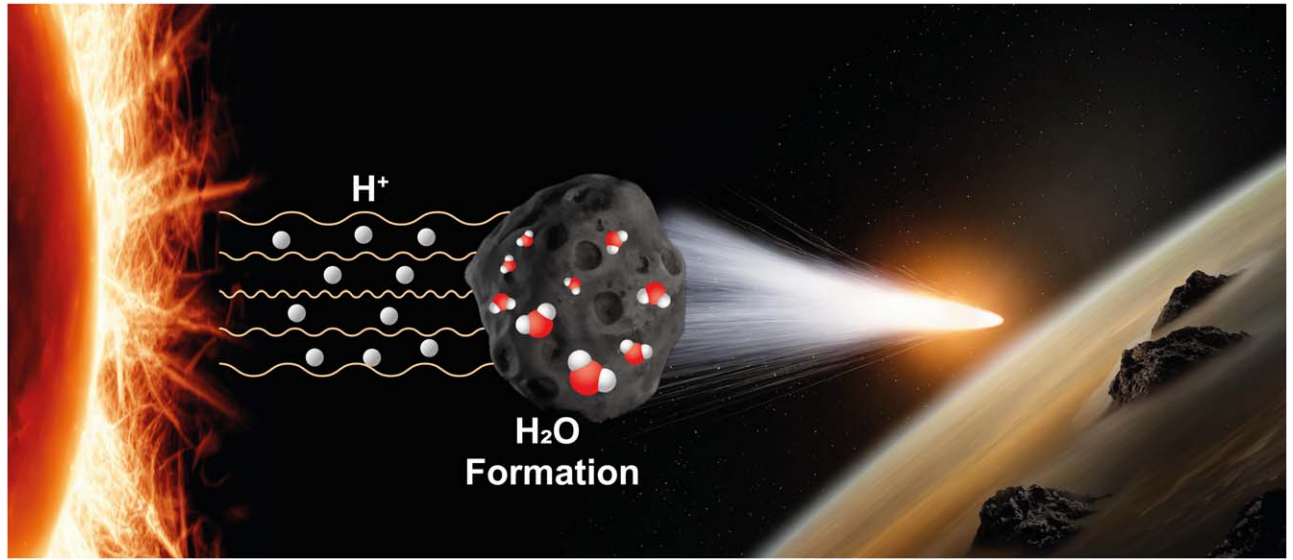


Figure 11. A schematic representation of water formation by solar wind on the surface of oxygen-containing minerals.

Table 3

Water Adsorption Capacity of Samples Treated by MW Discharge and the Amount of Accreted Material Required to Bring in One Equivalent of the Amount of Ocean Water on Earth

Sample	Ads. Capacity (wt%)	m_{tot} (kg)
Fe_2O_3	0.158	9.24×10^{19}
TiO_2 P25 anatase	0.262	5.57×10^{19}
Montmorillonite	0.152	9.61×10^{19}
Kaolinite	0.147	9.93×10^{19}
Augite	0.120	1.68×10^{19}
Diallage	0.685	3.30×10^{19}
Oligoclase	0.094	1.22×10^{20}
Al_2O_3	0.288	2.13×10^{19}
Olivine	0.148	1.55×10^{20}
RAS 445 meteorite	0.461	5.07×10^{19}
SAU 567 meteorite	0.154	3.17×10^{19}
TiO_2 nanorutile	0.442	9.86×10^{19}
TiO_2 anatase	0.087	9.48×10^{20}

composition than those pure minerals and natural samples investigated in our experiment. For comparison, J. J. Barnes et al. (2016) in their paper on the origin of water on the Moon show the water content (wt%) for various meteorite classes (see their Table 1). Of those, enstatite chondrites resemble the Earth's mantle's isotopic composition the most (L. Piani et al. 2020). They are the meteorite class with the least amount of water, at <0.05 wt%. On the other hand, CI chondrites are the richest in bulk H_2O content, with 14.05 wt% in their structure. Our experiments with water adsorption show between 0.09 and 0.46 wt% adsorbed water on the surface of the minerals. This adsorbed water should add to the internal content of the minerals and, in this way, solar wind could contribute to the Earth's water reservoir.

Besides material acquired by the Earth during accretion, the solar wind origin of water and its delivery to Earth could have gone on even during post-accretionary bombardment. M. Ferus et al. (2021) show that the Moon-accreted mass after the

formation of the Earth fell from 10^{16} to 10^6 kg yr^{-1} , with the exception of the Late Heavy Bombardment. Model estimates (e.g., H. F. Levison et al. 2001) show that asteroid and comet impacts during the classical Late Heavy Bombardment would bring in about $\sim 10^{20} \text{ kg}$ of material. If that material's surface was fully saturated with adsorbed water as composed of one of our minerals, our calculations suggest that at least one ocean equivalent of water could have been brought in. Again, of course, the outcomes of this scenario serve as a constraint on the delivered mass. In the case of the two meteorites, RAS 445 is an L3 ordinary chondrite and SAU 567 is a H3 ordinary chondrite. These are according to J. J. Barnes et al. (2016) low in water content (<1.11%).

This section serves as illustrative for the amount of required impacted mass. Better constraints as well as deeper discussion on this topic are out of the scope of this paper, which is mainly experimental.

6. Conclusions

The results of experiments summarized in this work, focused on surface bombardment with hydrogen atoms, clearly confirm the theory of the interaction of excited hydrogen or deuterium Rydberg atoms and ions with the surface oxygens of oxide minerals. Our experiments attempt to explain the origin of water in the areas of oxygen-containing solid material (e.g., dust, meteoroids, asteroids, comets) exposed to a stream of charged particles close to a parent star. This scenario is also applicable to the origin of water on Earth. Fourteen oxygen-containing minerals and samples, including two meteorite samples (RAS 445 and SAU 567), were shown to have a water adsorption capacity between 0.09 and 0.7 wt%. Water molecules are subsequently adsorbed on the surface of natural or synthetic minerals, including the surfaces of the selected meteorites. We used two independent methods for water detection in this work: TPD and FTIR. TPD experiments revealed broad water desorption peaks from temperatures of 400 K. While desorption at temperatures near 400 K can be caused by desorption of water formed during H/D bombardment, desorption of water molecules at higher temperatures can be caused by temperature-induced diffusion of implanted ions

and subsequent reaction with oxide oxygen during heating of the sample. This reaction could be an additional route for water formation. Due to this effect, a water molecule can be adsorbed on the surface of oxygen-containing particles and then transported over long distances and times.

Acknowledgments

The authors acknowledge the assistance received through the research infrastructure NanoEnviCz supported by the Ministry of Education, Youth, and Sports of the Czech Republic under Project No. LM2023066.

Appendix A Formation of Water in a MW Discharge: Further Spectra

Shown below are three figures (Figures 12, 13 and 14) with IR spectra that show the formation of D_2O on the surface of various minerals listed in Table 1 in the main text.

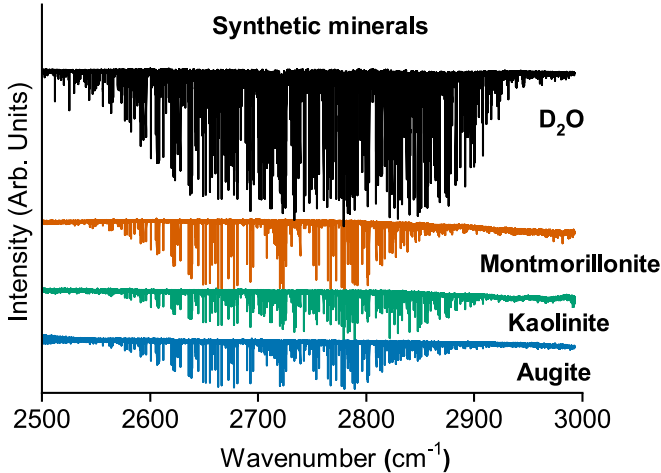


Figure 12. MW-FTIR experiment, in which different types of synthetic minerals were bombarded by deuterium atoms generated in a MW plasma. The gas-phase absorption spectrum of D_2O is depicted for comparison (in blue).

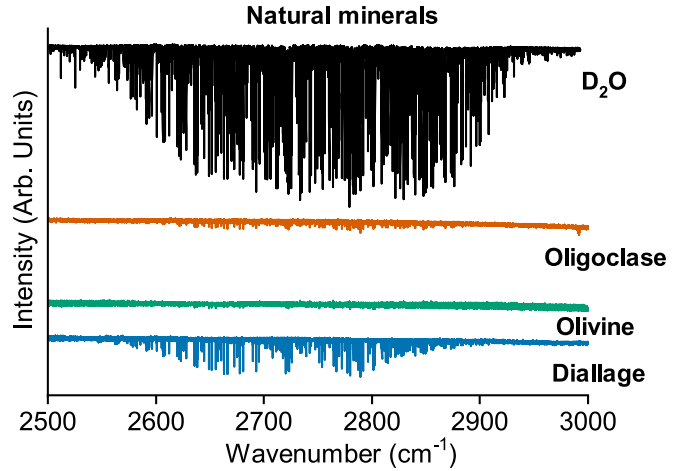


Figure 13. MW-FTIR experiment, in which different types of natural minerals were bombarded by deuterium atoms generated in a MW plasma. The gas-phase absorption spectrum of D_2O is depicted for comparison (in blue).

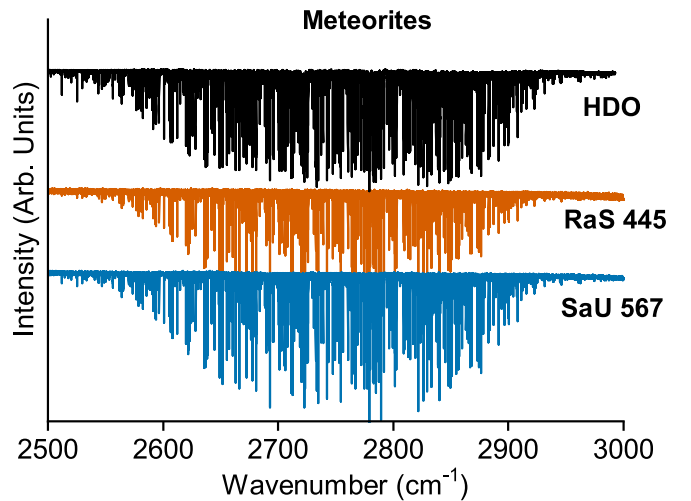


Figure 14. MW-FTIR experiment, in which selected meteorites were bombarded by deuterium atoms generated in a MW plasma. The gas-phase absorption spectrum of D_2O is depicted for comparison (in blue).

Appendix B MW-FTIR Experiment

Figure 15 shows a photo of the MW-FTIR experiment. Central to this figure is the sample cell. From the right, it consists of a stopcock for gas inlet, a part with infrared-transparent windows used for measurement of the content of D₂O and the part with the sample. At the bottom of the picture, there is a red infrared radiation source. Opposite to this at the top is the spectrometer with an entry window. Finally, the gray object on the left is the furnace used for heating the samples as described in the main text.

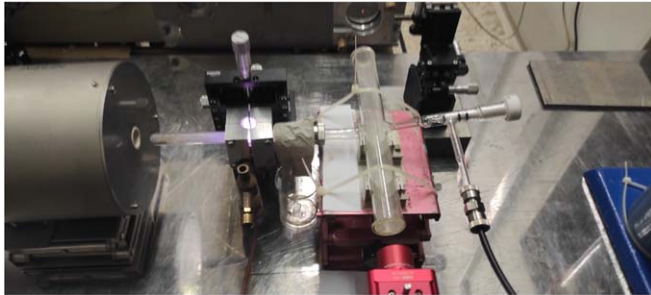


Figure 15. Photo of the MW-FTIR experiment. The central object in this picture is the sample cell. The MW discharge is seen radiating a pink glow. The gray object on the left is a high-temperature oven. On the right side, a valve and a black gas line are visible. The red object at the bottom is then an IR radiation source; opposite the cell on the top side is an entry window into the spectrometer.

Appendix C Rydberg Hydrogen Spectrum

Figure 16, shows a hydrogen atomic spectrum measured on our Bruker IFS 120 spectrometer during the experiment in emission mode. This spectrum confirms the presence of excited hydrogen atoms in the sample during the discharge. Detailed description of the hydrogen atomic spectrum can be found in G. Herzberg & C. Jungen (1982) and C. Jungen et al. (1989, 1990).

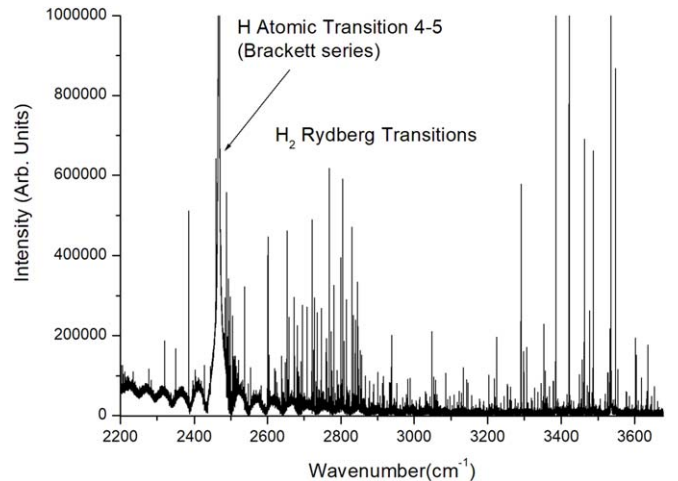


Figure 16. High-resolution emission MW discharge spectrum of pure hydrogen. Details are given in G. Herzberg & C. Jungen (1982) and C. Jungen et al. (1989, 1990).

Appendix D Blank Experiments

Figure 17 shows absorption spectra recorded for all samples in the MW-FTIR experiments. The samples in this blank experiment were not exposed to the MW discharge, but otherwise were treated as in the regular experiment. No water was observed.

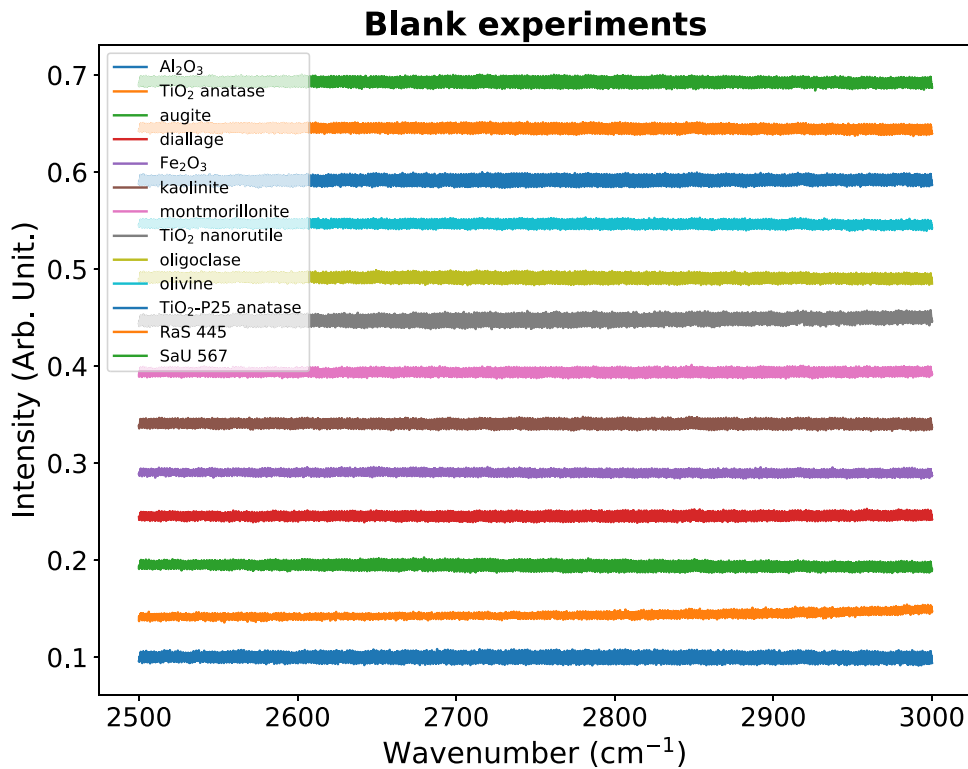


Figure 17. MW-FTIR experiment, blank experiments. The figure shows FTIR spectra of samples not exposed to the MW discharge in the MW-FTIR experiments. No absorption at all is visible, meaning that no water was present.

ORCID iDs

- Svatolpuk Civiš <https://orcid.org/0000-0001-6215-0256>
 Jiří Kubišta <https://orcid.org/0000-0002-5746-9315>
 Jan Plšek <https://orcid.org/0000-0003-4706-0097>
 Antonín Knížek <https://orcid.org/0000-0002-0932-0380>

References

- Alexander, C. M. O., Bowden, R., Fogel, M. L., et al. 2012, *Sci.*, **337**, 721
 Altweig, K., Balsiger, H., Bar-Nun, A., et al. 2015, *Sci.*, **347**, 1261952
 Bandfield, J. L. 2002, *JGRE*, **107**, 5042
 Bandfield, J. L., Poston, M. J., Klima, R. L., & Edwards, C. S. 2018, *NatGe*, **111**, 173
 Barnes, J. J., Kring, D. A., Tartèse, R., et al. 2016, *NatCo*, **7**, 11684
 Bradley, J. P., Ishii, H. A., Gillis-Davis, J. J., et al. 2014, *PNAS*, **111**, 1732
 Civiš, S., & Knížek, A. 2021, *ESC*, **5**, 1172
 Civiš, S., Knizek, A., Ivanec, O., et al. 2017, *NatAs*, **1**, 721
 Civiš, S., Bousa, M., Zukal, A., et al. 2016, *JPCC*, **120**, 508
 Daly, L., Lee, M. R., Hallis, L. J., et al. 2021, *NatAs*, **5**, 1275
 Eidsvag, H., Bentouba, S., Vajeeston, P., Yohi, S., & Velauthapillai, D. 2021, *Molecules*, **6**, 26
 Ferus, M., Heays, A. N., & Knížek, A. 2021, Comprehensive Series in Photochemical and Photobiological Sciences (Cambridge: The Royal Society of Chemistry), 239
 Fujishima, A., & Honda, K. 1972, *Natur*, **238**, 37
 Gordon, I. E., Rothman, L. S., Hargreaves, R. J., et al. 2022, *JQSRT*, **277**, 107949
 Greenwood, J. P., Itoh, S., Sakamoto, N., et al. 2011, *NatGe*, **4**, 79
 Hallis, L. J., Huss, G. R., Nagashima, K., et al. 2015, *Sci.*, **350**, 795
 Heays, A. N., 2022 spectr, <https://github.com/ahheays/spectr>
 Hersant, F., Gautier, D., & Hure, J.-M. 2001, *ApJ*, **554**, 391
 Herzberg, G., & Junge, C. 1982, *JChPh*, **77**, 5876
 Hirschmann, M. M. 2016, *AmMin*, **101**, 540
 Ichimura, A. S., Zent, A. P., Quinn, R. C., Sanchez, M. R., & Taylor, L. A. 2012, *E&PSL*, **345–348**, 90
 Izidoro, A., & Piani, L. 2022, *Eleme*, **18**, 181
 Jiang, Q., Karato, S.-i., Bissbort, T., & Foteinou, V. 2024, *Icar*, **411**, 115958
 Junge, C., Dabrowski, I., Herzberg, G., & Kendall, D. J. W. 1989, *JChPh*, **91**, 3926
 Junge, C., Dabrowski, I., Herzberg, G., & Vervloet, M. 1990, *JChPh*, **93**, 2289
 Laferriere, K. L., Sunshine, J. M., & Feaga, L. M. 2022, *JGRE*, **127**, e07361
 Levison, H. F., Dones, L., & Duncan, M. J. 2001, *AJ*, **121**, 2253
 Li, R., Weng, Y., Zhou, X., et al. 2015, *Energy Environ. Sci.*, **8**, 2377
 Liu, Y., Guan, Y., Zhang, Y., et al. 2012, *NatGe*, **5**, 779
 Lucey, P., Korotev, R. L., Gillis, J. J., et al. 2006, *RvMG*, **60**, 83
 Lucey, P. G., Petro, N., Hurley, D. M., et al. 2022, *ChEG*, **82**, 125858
 Macounová, K. M., Klusáčková, M., Nebel, R., et al. 2017, *JPCC*, **121**, 6024
 Marty, B. 2012, *E&PSL*, **313-314**, 56
 McCubbin, F. M., & Barnes, J. J. 2019, *E&PSL*, **526**, 115771
 Meadows, V., Arney, G., Schmidt, B., & Des Marais, D. J. 2020, Planetary Astrobiology (Tucson, AZ: Arizona Univ. Press), 522
 Morbidelli, A., Chambers, J., Lunine, J. I., et al. 2000, *M&PS*, **35**, 1309

- O'Brien, D. P., Walsh, K. J., Morbidelli, A., Raymond, S. N., & Mandell, A. M. 2014, *Icar*, **239**, 74
- Paquette, J. A., Fray, N., Bardyn, A., et al. 2021, *MNRAS*, **504**, 4940
- Piani, L., Marocchi, Y., Rigaudier, T., et al. 2020, *Sci*, **369**, 1110
- Piani, L., Marocchi, Y., Vacher, L. G., Yurimoto, H., & Bizzarro, M. 2021, *E&PSL*, **567**, 117008
- Pieters, C. M., Goswami, J. N., Clark, R. N., et al. 2009, *Sci*, **326**, 568
- Raymond, S. N., & Izidoro, A. 2017, *SciA*, **3**, e1701138
- Raymond, S. N., Quinn, T., & Lunine, J. I. 2006, *Icar*, **183**, 265
- Roberts, H., Herbst, E., & Millar, T. J. 2004, *A&A*, **424**, 905
- Schaible, M. J., & Baragiola, R. A. 2014, *JGRE*, **119**, 2017
- Sorescu, D. C., Civiš, S., & Jordan, K. D. 2014, *JPCC*, **118**, 1628
- Sunshine, J. M., Farnham, T. L., Feaga, L. M., et al. 2009, *Sci*, **326**, 565
- Thomas, C. 1994, International Affairs, Vol. 70 (New York: Oxford Univ. Press), 557
- Vattuone, L., Smerieri, M., Savio, L., et al. 2013, *RSPTA*, **371**, 20110585
- Walsh, K. J., Morbidelli, A., Raymond, S. N., O'Brien, D. P., & Mandell, A. M. 2011, *Natur*, **475**, 206
- Yang, H. G., Sun, C. H., Qiao, S. Z., et al. 2008, *Natur*, **453**, 638
- Zhu, C., Crandall, P. B., Gillis-Davis, J. J., et al. 2019, *PNAS*, **166**, 11165